Two-dimensional Rare-earth-based Half-metals with Topological Bimerons

Weiqi Liu[1,2], *Xue He*[1,2], *Jianxiong Zhang*[1,2], *Fengshan Zheng*[1,2,3], *Yu-Jun Zhao*[2], *Rui Wu*[1,2,3]*, *Jinbo Yang*[4], *Mathias Kläui*[5], *Yanglong Hou*[6,7]*

1. Spin-X Institute, South China University of Technology, Guangzhou 511442, China

2. School of Physics and Optoelectronics, South China University of Technology, Guangzhou 511442, China

3. State Key Laboratory of Luminescent Materials and Devices, South China University of Technology, Guangzhou 511442, China

4. State Key Laboratory for Mesoscopic Physics, School of Physics, Peking University, Beijing 100871, China

5. Institute of Physics, Johannes Gutenberg-University Mainz, Staudingerweg 7, Mainz 55128, Germany

6. School of Materials, Shenzhen Campus of Sun Yat-Sen University, Shenzhen 518107, China

7. School of Materials Science and Engineering, Beijing Key Laboratory for Magnetoelectric Materials and Devices, Peking University, Beijing 100871, China

**E-mail: ruiwu001@scut.edu.cn; hou@ sysu.edu.cn*

Abstract

Two-dimensional magnets with spontaneous topological spin textures have important application prospects in highly integrated spintronic devices. However, so far, the predicted two-dimensional magnets with topological spin textures are majorly based on transition metals, and most of them are semiconductors or metals. Here, based on first-principles calculations, we predict two-dimensional rare-earth-based half-metallic monolayer GdA_2N_4 (A=Ge, Sn), with 100% spin polarization. Spontaneous topological spin textures, i.e., bimerons clusters, are revealed in those monolayers due to the magnetic frustration and easy-plane magnetic anisotropy. The bimerons clusters can be efficiently tunned through biaxial strain and driven by in-plane spin-polarized current. These results underscore the promising potential of rare-earth-based two-dimensional half-metals for spintronic devices applications.

Introduction

Inspired by the pioneering work of monolayer van der Waals (vdW) materials CrI_3[1] and bilayer $Cr_2Ge_2Te_6$[2], extensive research has been greatly stimulated on this type of materials. Results on a range of magnetic vdW magnets, such as VSe_2[3], $CrPS_4$[4], $CuCrP_2S_6$[5], Fe_3GeTe_2[6] and Fe_3GaTe_2[7] etc., have been reported, which provide an ideal research platform for low dimensional magnetism. In the few-layer vdW magnets, large spin-filtering tunnelling magnetoresistance[8, 9], strain induced antiferromagnetic (AFM) – ferromagnetic (FM) transition, and large electric field tunability of magnetism[10, 11] , and the layer-number and twist-angle dependence of magnetism[1, 12] have been reported, which is highly preferred in the spintronic devices. Recently, various intriguing physical properties such as anomalous valley Hall effect[13, 14], topological spin textures[15-17] and altermagnetism[18] in two-dimensional (2D) magnetic materials have also reported and received widespread attention. For heterostructures of FM and AFM 2D materials, exchange bias has been explored[19, 20].

Various topologically nontrivial spin textures, such as skyrmions[15, 21], bimerons[22, 23] and hopfions[24, 25], are topologically stabilized and can be effectively manipulated[26, 27], making them promising information carriers for future high-density storage and information processing devices. Recently, great strides have been made to discover new topological spin textures in vdW or 2D magnets[16, 28-30]. The magnetic skyrmions have been experimentally demonstrated in vdW ferromagnets Fe_3GeTe_2, Fe_5GeTe_2 and Fe_3GaTe_2 flakes[16, 17, 30, 31]. Current-induced magnetic skyrmions or skyrmionium motion in Fe_3GaTe_2 flakes has also been observed at room temperature[32, 33]. Besides, various monolayer systems have also been theoretically predicted to stabilize topological spin textures. For instance, spontaneous antiskyrmions are predicted in monolayer NiI_2 due to the magnetic frustration[28]. Meron-like topological spin textures have been predicted in XY-type magnet monolayer $CrCl_3$ as a result of the easy-plane magnetic anisotropy induced by magnetic dipole-dipole interaction[34]. However, so far, topological spin textures are mostly reported in magnetic semiconductors[35-38], metals[39-43], while rarely reported in intrinsic half-metals, especially for 2D magnets.

Topological spin textures can be more effectively driven by 100% spin-polarized current in half-metallic systems. Moreover, most 2D magnetic systems with topological spin textures are based on transition metals[37, 38, 41], and the 4*f*-electrons based 2D magnetic systems that exhibit topological spin textures are still in demand. Theoretical studies suggest rare-earth-based 2D magnets show large atomic magnetic moment and strong magnetic anisotropy[44-49], which is crucial for spintronic devices applications. Experimental studies have shown that the complex magnetic interactions of the 4*f* electron systems are the reason for the emergence of topological spin textures in rare-earth-based magnets[50-52]. For example, in $Tb_6Co_{2.17}Si_{2.5}$ magnet[52], the 4*f* electrons play an important role in the formation of (anti)meron chains. In $Tm_3Fe_5O_{12}$/Pt heterostructures[53], skyrmions are stabilized by the interfacial Dzyaloshinskii–Moriya interaction (DMI). Therefore, exploring the topological spin textures in 2D half-metallic systems based on rare-earth elements is of great significance.

Inspired by the successful synthesis of monolayer $MoSi_2N_4$[54], which exhibit exotic physical properties[55-58], here we explore and predicted a new stable rare-earth-based monolayer GdA_2N_4 (A=Ge, Sn). It is shown that monolayer GdA_2N_4 is intrinsic XY-type FM half-metals with easy-plane magnetic anisotropy. Spontaneous bimerons are revealed using micromagnetic simulations, which is ascribed to the magnetic frustration and easy-plane magnetic anisotropy. Different types of bimerons are induced by biaxial strain. In addition, highly efficient electric driven motion of bimerons clusters is achieved. Our results pave a new avenue for the future application of 2D rare-earth-based half-metallic materials in the spintronics.

Results and discussion

Monolayer GdA_2N_4 has a hexagonal crystal structure. According to the structure of the intermediate layer GdN_2, it can be categorized into 1T and 2H-GdA_2N_4 phases with p3m1 and p-6m2 space groups[55], as illustrated in Figure 1(a) and Figure S2, respectively (see details of the calculation in the supplementary materials). Firstly, we conduct complete structural optimization and calculate the relative energy and magnetic ground state of the 1T and 2H-GdA_2N_4 phases, respectively. The results are detailed in

Table S2, both 1T and 2H-GdA_2N_4 phases exhibit a FM ground state, and the 1T phase has lower energy compared to the corresponding 2H phase. The energy difference between 1T and 2H phases is akin to that of dihalides monolayer MX_2 (M=Cr, Mn, Fe, Co and X=Cl, Br, I)[59]. Therefore, unless otherwise specified, all study in the following is focused on the 1T phase. The lattice constants of monolayer $GdGe_2N_4$ and $GdSn_2N_4$ after optimization are 3.251 and 3.488 Å, respectively. The lattice constants increase proportionally with the element number of A (Ge→Sn). In addition, we calculate the cohesive energy, formation energy, elastic constants, phonon dispersion spectra and ab initio molecular dynamics (AIMD) simulations of the system to confirm its stability, as shown in supplemental material Figure S3-S5, providing guidance for experimental synthesis.

Based on the calculated stable structure of monolayer GdA_2N_4, we investigate the electronic and magnetic properties of the system. As shown in Figure S6, we construct three different magnetic configurations, i.e., FM, stripe-antiferromagnetic (s-AFM), and zigzag-antiferromagnetic (z-AFM) states. The results show that the energy difference $\Delta E = E_{z-AFM} - E_{FM}$ for monolayer $GdGe_2N_4$ and $GdSn_2N_4$ is 105.8 and 101.3 meV/f.u. (formula unit), respectively, exhibiting FM ground state. As shown in Figure 1(b), the density of states (DOS) of monolayer $GdGe_2N_4$ are calculated, which shows that monolayer $GdGe_2N_4$ exhibits half-metallic properties. The Fermi level only crosses the spin-down channel, while the spin-up channel exhibits a band gap, as shown in Figure 1(c) of the schematic diagram. This characteristic is valuable for applications requiring 100% spin-polarized current, such as spin filters and spin valves. As shown in Figure 1(d), the spin resolved band structure further confirms the half-metallic properties. The monolayer $GdSn_2N_4$ has similar half-metallic properties, except that the bandgap value of the spin-up channel is slightly smaller than that of monolayer $GdGe_2N_4$ (see Figure S7). In addition, the monolayer GdA_2N_4 have a total magnetic moment of $8\mu_B$/f.u. which primarily originates from the spin magnetic moment of Gd-$4f$ electrons, as shown in Figure S8 and Figure S9.

According to the Mermin-Wagner theorem[60], magnetic anisotropy is crucial in the establishment of long-range magnetic ordering. Large magnetic anisotropy can counteract thermal fluctuations, thereby enhancing the durability of magnetic data storage. The magnitude of magnetic anisotropy can be represented by magnetic anisotropy energy (MAE). Given the strong spin orbit coupling (SOC) effect of Gd atom, potentially resulting in a large MAE[44], we calculate the MAE of monolayer GdA_2N_4 by using the formula, $\mathrm{MAE} = \mathrm{E_x} - \mathrm{E_z}$, where $\mathrm{E_x}$ and $\mathrm{E_z}$ represent the total energy of magnetization direction along the in-plane *x* direction and out-of-plane *z* direction, respectively. The positive (negative) MAE indicates that the system shows easy-axis (easy-plane) magnetic anisotropy. As shown in Figure 2(a), MAE values along different rotation angle θ within the *xy*, *yz*, and *xz* planes have been calculated. The relationship between MAE and rotation angle θ can be fitted using the equation, $\mathrm{MAE}(\theta) = \mathrm{K_1}\sin^2\theta + \mathrm{K_2}\sin^4\theta$, where $\mathrm{K_1}$ and $\mathrm{K_2}$ are magnetic anisotropy coefficients. As exhibited in Table S4, the negative $\mathrm{K_1}$ indicates that monolayer $GdGe_2N_4$ exhibits easy-plane magnetic anisotropy. In the *xy* plane, various magnetization orientations yield identical MAE, signifying the absence of in-plane anisotropy within this system. Therefore, the monolayer $GdGe_2N_4$ can be classified as the 2D XY magnet[46]. As shown in Figure 2(b), the monolayer $GdGe_2N_4$ has -1290 μeV/f.u. magnetic anisotropy. The value is larger compared to monolayer GdI_2 (-553 μeV/Gd)[44] and CeI_2 (-234 μeV/Ce)[46]. The monolayer $GdSn_2N_4$ also belongs to the XY magnet and has higher MAE (-2046 μeV/f.u.) than monolayer $GdGe_2N_4$, and the results are shown in Figure S10(a-b). Note that for thin film flakes, additionally a shape anisotropy contributes that also favors an easy-plane magnetic order.

The magnetic ordering temperature of the GdA_2N_4 system is studied next. Notably, monolayer GdA_2N_4 with in-plane easy magnetization axis exhibits a Berezinskii-Kosterlitz-Thouless (BKT) magnetic phase transition[61, 62]. The critical temperatures $\mathrm{T_c}$ of BKT magnetic transition can be estimated using the equation[63, 64], $\mathrm{T_c} = (0.89\Delta\mathrm{E})/(8\mathrm{k_B})$, where $\mathrm{k_B}$ is the Boltzmann constant. The estimated $\mathrm{T_c}$ of monolayer $GdGe_2N_4$ and $GdSn_2N_4$ are 136.6 and 130.7 K, respectively, which is much larger than the $\mathrm{T_c}$ of the XY-type monolayer $CrCl_3$ (12 K)[34], and is close to the $\mathrm{T_c}$ of the XY-type bilayer $NiPS_3$ (150 K)[65, 66].

Typically, 2D materials with easy-plane magnetic anisotropy yield a residual SO(2) symmetry that usually lead to nonlinear spin textures, such as magnetic vortex and antivortex[34]. Through calculating the total energy of different magnetic configurations (detailed in Figure S6), the nearest neighbor and second nearest neighbor exchange coupling constants J_1 (J_2) of monolayer GdA_2N_4 are calculated, the results are detailed in Table S4. The frustration presents in this system due to the different signs of J_1 and J_2. The magnetic frustration ratio, defined as $|J_2|/J_1$, of monolayer $GdGe_2N_4$ and $GdSn_2N_4$ is about 0.33 and 0.32, respectively, which is slightly greater than the values of monolayer CrTeI (0.29) and MnPCl (0.27)[67]. With considering both the strong easy-plane magnetic anisotropy and large magnetic frustration ratio, micromagnetic simulations reveal that monolayer GdA_2N_4 exhibits spontaneous bimerons at zero magnetic field. As shown in Figure 2(c), the self-assembled antiparallel arranged bimerons are observed in monolayer $GdGe_2N_4$, which have also been reported in 2D magnetic systems, such as monolayer $CrCI_3$[34], CrTeI and MnPCl[67]. In addition, the bimerons in monolayer $GdSn_2N_4$ exhibit a linear alignment (see Figure S10(c)). The topological charge density is defined as $\mathrm{q} = \frac{1}{4\pi}\mathbf{S} \cdot (\partial_x \mathbf{S} \times \partial_y \mathbf{S})$[68]. The topological charge Q is defined as $\mathrm{Q} = \int \mathrm{q}\mathrm{d}x\mathrm{d}y$[36]. Figure 2(d) and Figure S10(d) show the distribution of topological charge density for monolayer GdA_2N_4, the bimerons with Q=1 are composed of a pair of merons with Q=1/2. As the topological counterpart of the skyrmions, bimerons carry an integer topological charge Q in the in-plane magnetized system[27, 69]. In Figure S11, we conduct a more detailed discussion on the mechanism of magnetic frustration in this system and its effect on the formation of topological spin textures.

To tune the properties and in particular the spin textures, we investigate the impact of strain on the topological spin textures of the monolayer GdA_2N_4. Firstly, we find that for biaxial strain as shown in Figure 3(a) and Figure S12(a), the band gap value of the spin-up channel for monolayer GdA_2N_4 under compressive strain increases, indicating the enhancement of the half-metallic characteristics. However, the band gap value of the spin-up channel for monolayer GdA_2N_4 decreases under tensile strain, leading to the transition of monolayer $GdGe_2N_4$ and $GdSn_2N_4$ from half-metals to normal metal states at a critical strain of 5% and 3%, respectively, as shown in Figure S13. In addition, as shown in Figure S14, the monolayer GdA_2N_4 maintains the FM ground state under different biaxial strain. Through calculating the total energy of different magnetic configurations, the corresponding magnetic frustration ratio values of monolayer GdA_2N_4 under varying biaxial strain are shown in Figure 3(b) and Figure S12(b). It is observed that the value increases to about 0.5 under the 5% tensile strain, while the value slightly decreases under compressive strain. Figure 3(c) shows the MAE of monolayer $GdGe_2N_4$ under varying biaxial strain. The MAE increases to about -3000 μeV/f.u. under -5% compressive strain, while the MAE decreases under tensile strain. It is worth noting that monolayer $GdGe_2N_4$ exhibits a MAE of 94 μeV/f.u. under 5% tensile compressive strain, indicating a dominating perpendicular magnetic anisotropy (PMA) at this strain level. The MAE of monolayer $GdSn_2N_4$ under strain is similar to monolayer $GdGe_2N_4$, but its magnetic anisotropy remains in-plane, as shown in Figure S12(c). Through second-order perturbation theory analysis[70], biaxial strain significantly affects the MAE of monolayer GdA_2N_4 by changing the matrix element difference (p_y, p_z) of Gd atom. The specific results and discussion can be found in the supplemental materials and Figures S15-S17. As shown in Figure 3(d) and Figure S12(d), these unique topological spin textures can be significantly modified via the biaxial strain.

The changes of the magnetic properties affect the stable spin textures. In particular, bimerons clusters can be induced under compressive strain through decreasing the magnetic frustration ratio and increasing the easy-plane magnetic anisotropy, while the tensile strain induces bimerons chains through increasing magnetic frustration ratio and weakening easy-plane magnetic anisotropy. Notably, due to the presence of PMA in monolayer $GdGe_2N_4$ under 5% tensile strain, a so-called Bloch line configuration is also stabilized, as shown in Figure 3(d). Figure S18 shows the topological charge density of monolayer GdA_2N_4 under biaxial strain, due to the presence of easy-plane magnetic anisotropy. It is worth noting that bimerons clusters with opposite signs of topological charge can coexist with each other[71, 72]. The bimerons composed of a pair of merons Q=-1/2 are called an antibimerons with Q=-1. The bimerons and antibimerons with the same absolute value of Q have different out-of-plane spin configurations[73]. The recent theories have predicted a topological spin textures hybrid-meron with a topological charge of Q=0[69], which still exhibits topologically nontrivial due to the AFM coupling effect of interlayer bimerons. The influence of dipole-dipole interaction on the topological spin textures is also discussed in Supplementary Information (Figure S19).

2D half-metals can provide 100% spin-polarized current, which is crucial for efficient manipulation of topological spin textures. Thus, we further discuss the dynamics of topological spin textures caused by the spin-transfer torque[74]. The spin-transfer torque can simulate the in-plane spin-polarized current[75]. The motion of topological spin textures driven by in-plane current due to spin transfer torques can be described by the Thiele equation[26, 76]:

$$\mathbf{F} + \mathbf{G} \times (\mathbf{u} - \mathbf{v}) + \mathcal{D}(\beta\mathbf{u} - \alpha\mathbf{v}) = 0 \tag{1}$$

Where $\mathbf{F}$ is the effective force[77]. $\mathbf{G} = (0,\ 0, -4\pi Q)$ is the gyromagnetic coupling vector[73]. $\mathbf{u}$ is the spin drift velocity related to spin-polarized current; $\mathbf{v}$ is the spin structure drift velocity and β is the nonadiabaticity constant[78]. $\mathcal{D}$ is the dissipative force, where $\mathcal{D}_{\mathrm{ij}} = \frac{1}{4\pi}\int \mathrm{dxdy}\, \partial_{\mathrm{i}}\mathbf{S} \cdot \partial_{\mathrm{j}}\mathbf{S}$. When considering the direction of the spin-polarized current along the *x* axis, with $\mathbf{u}_{\mathrm{y}} = \mathbf{0}$, the drift velocity component of the topological spin textures driven by the current is[24, 75]:

$$\begin{aligned} \mathbf{v}_{\mathrm{x}} &= \left(\frac{\beta}{\alpha} + \frac{G^2}{\alpha}\frac{\alpha-\beta}{G^2+\alpha^2\mathcal{D}^2}\right)\mathbf{u}_{\mathrm{x}} \\ \mathbf{v}_{\mathrm{y}} &= \left(\mathcal{D}G\frac{\alpha-\beta}{G^2+\alpha^2\mathcal{D}^2}\right)\mathbf{u}_{\mathrm{x}} \end{aligned} \tag{2}$$

Note that topological spin textures will exhibit transverse motion induced by the Magnus force under the spin-polarized current, i.e., Hall-like effect[27]. The Hall angle $\theta=\arctan(v_y/v_x)$. Here, we investigate the dynamics of bimerons clusters under spin-polarized current. The consistency between analytical results and numerical results is verified through the simulation results of isolated bimerons, as shown in Figure S20. Figure 4(a-h) show the snapshots of the topological spin textures of monolayer GdA_2N_4 with bimerons clusters under different biaxial strain driven by spin-polarized current along *y* axis. The topological spin textures with different topological charge numbers all exhibit a linear motion trajectory. However, it is worth noting that the opposite Q signs lead to the opposite transverse velocity v_x. As shown in Figure 4(a) and Figure S21, the bimerons clusters with negative topological charge numbers are subjected to a Magnus force to the right, resulting in a drift velocity component v_x to the right. In contrary, for bimerons clusters with positive topological charge numbers (see Figure 4(b-h)), they are subjected to a Magnus force to the left during the drift process, resulting in a drift velocity component v_x to the left. As shown in Figure 4(i), it can be seen that although the absolute values of the drift velocity components of bimerons clusters with different topological charge numbers are slightly different, the absolute values of Hall angle for all bimerons clusters are within the range of 11° to 11.6° (see Figure 4(j)), indicating that the bimerons Hall effect does not depend strongly on the size and shape. According to formula (2), the Hall angle of the system is determined by $\frac{\mathcal{D}}{G}$, as shown in Figure 4(j), the dissipation force $\mathcal{D}$ is proportional to the topological charge Q, therefore, the bimeron clusters with different topological charge numbers exhibit similar Hall angle. In addition, the influence of nonadiabaticity constant β on Hall angle is also discussed in Supplementary Information (Figures S22-S23).

Based on the above results analysis, with applying spin-polarized current in an appropriate direction, the collision between bimerons clusters with opposite signs of the topological charge can be achieved. The Figure S24(a-f) show the snapshots of the topological spin textures of monolayer $GdGe_2N_4$ under -3% compressive strain driven by spin-polarized current, the bimerons clusters with topological charge Q=9 and -3 collide and the system energy undergoes a drastic change between 200-300 ns (see Figure S24(g)), indicating the collision and merging between the bimerons clusters with opposite topological charge signs and resulting the new bimerons clusters with topological charge Q=6. It is worth noting that this process entails topological charge numbers conservation in the system, as shown in the Figure S24(h).

With these findings, we evidence the stability of bimerons in monolayer GdA_2N_4 systems with half-metallic properties. The dynamics due to injected fully polarized currents as analyzed within the Thiele model, shows that bimerons clusters with different topological charge numbers exhibit a similar Hall effect, and collision and merging between the spin textures can be achieved through injection of currents while conserving the overall topological winding number of the system.

Conclusion

We use first-principles calculations to predict monolayer GdA_2N_4 (A=Ge, Sn) with a seven atom layers structure, and systematically study its stability, electronic, and magnetic properties. It is found that monolayer GdA_2N_4 exhibits half-metallicity and easy-plane magnetic anisotropy. Monolayer GdA_2N_4 exhibits spontaneous bimerons, which is induced by magnetic frustration and easy-plane magnetic anisotropy. The morphology of the topological spin textures can be efficiently tuned through applied biaxial strain. The half metallic electronic structure naturally lends the system to manipulation by injected currents. The dynamics of micromagnetic simulations indicate that the bimerons clusters show a linear motion under injected spin-polarized currents. The absolute value of bimerons Hall angle does not depend strongly on the size and shape. In addition, new bimerons clusters can be obtained through collision and merging between bimerons clusters that could be useful for complex computational approaches. With the above intriguing properties, the predicted rare-earth 2D magnets with half-metallic properties are particularly promising for spintronic devices like spin transfer torques driven magnetic tunneling junction and race-track memories.

Acknowledgement

This work is supported by the National Key R&D Program of China (grant no. 2022YFA1203902, 2022YFA1200093), the National Natural Science Foundation of China (NSFC) (grant nos. 12241401, 12374108 and 12104052, 52373226, 52027801, 92263203), and the China-Germany Collaboration Project (M-0199), the Fundamental Research Funds for the Central Universities, and the State Key Lab of Luminescent Materials and Devices, South China University of Technology. We acknowledge support by the German Research Foundation (CRC TRR 288 - 422213477 Project A12). This work is partially supported by High Performance Computing Platform of South China University of Technology.

Reference

[1] Huang, B.; Clark, G.; Navarro-Moratalla, E., et al. Layer-dependent ferromagnetism in a van der Waals crystal down to the monolayer limit. *Nature*, **2017**, *546* (7657), 270-273.

[2] Gong, C.; Li, L.; Li, Z., et al. Discovery of intrinsic ferromagnetism in two-dimensional van der Waals crystals. *Nature*, **2017**, *546* (7657), 265-269.

[3] Bonilla, M.; Kolekar, S.; Ma, Y., et al. Strong room-temperature ferromagnetism in VSe_2 monolayers on van der Waals substrates. *Nature Nanotechnology*, **2018**, *13* (4), 289-293.

[4] Wu, R.; Ross, A.; Ding, S., et al. Magnetotransport study of van der Waals $CrPS_4$/(Pt, Pd) heterostructures: Spin-flop transition and room-temperature anomalous Hall effect. *Physical Review Applied*, **2022**, *17* (6), 064038.

[5] Wang, X.; Shang, Z.; Zhang, C., et al. Electrical and magnetic anisotropies in van der Waals multiferroic $CuCrP_2S_6$. *Nature Communications*, **2023**, *14* (1), 840.

[6] Fei, Z.; Huang, B.; Malinowski, P., et al. Two-dimensional itinerant ferromagnetism in atomically thin Fe_3GeTe_2. *Nature Materials*, **2018**, *17* (9), 778-782.

[7] Zhang, G.; Guo, F.; Wu, H., et al. Above-room-temperature strong intrinsic ferromagnetism in 2D van der Waals Fe_3GaTe_2 with large perpendicular magnetic anisotropy. *Nature Communications*, **2022**, *13* (1), 5067.

[8] Song, T.; Cai, X.; Tu, M. W., et al. Giant tunneling magnetoresistance in spin-filter van der Waals heterostructures. *Science*, **2018**, *360* (6394), 1214-1218.

[9] Song, T.; Tu, M. W.; Carnahan, C., et al. Voltage control of a van der Waals spin-filter magnetic tunnel junction. *Nano Letters*, **2019**, *19* (2), 915-920.

[10] Jiang, S.; Li, L.; Wang, Z., et al. Controlling magnetism in 2D CrI_3 by electrostatic doping. *Nature Nanotechnology*, **2018**, *13* (7), 549-553.

[11] Jiang, S.; Shan, J.; Mak, K. F. Electric-field switching of two-dimensional van der Waals magnets. *Nature Materials*, **2018**, *17* (5), 406-410.

[12] Xu, Y.; Ray, A.; Shao, Y.-T., et al. Coexisting ferromagnetic–antiferromagnetic state in twisted bilayer CrI_3. *Nature Nanotechnology*, **2022**, *17* (2), 143-147.

[13] Tong, W.-Y.; Gong, S.-J.; Wan, X., et al. Concepts of ferrovalley material and anomalous valley Hall effect. *Nature Communications*, **2016**, *7* (1), 13612.

[14] Zhao, P.; Ma, Y.; Lei, C., et al. Single-layer $LaBr_2$: Two-dimensional valleytronic semiconductor with spontaneous spin and valley polarizations. *Applied Physics Letters*, **2019**, *115* (26),

[15] Ding, B.; Li, Z.; Xu, G., et al. Observation of magnetic skyrmion bubbles in a van der Waals ferromagnet Fe_3GeTe_2. *Nano Letters*, **2020**, *20* (2), 868-873.

[16] Birch, M. T.; Powalla, L.; Wintz, S., et al. History-dependent domain and skyrmion formation in 2D van der Waals magnet Fe_3GeTe_2. *Nature Communications*, **2022**, *13* (1), 3035.

[17] Liu, C.; Zhang, S.; Hao, H., et al. Magnetic skyrmions above room temperature in a van der Waals ferromagnet Fe_3GaTe_2. *Advanced Materials*, **2024**, *36* (18), 2311022.

[18] Zhu, Y.; Chen, T.; Li, Y., et al. Multipiezo effect in altermagnetic V_2SeTeO monolayer. *Nano Letters*, **2024**, *24* (1), 472-478.

[19] Puthirath Balan, A.; Kumar, A.; Reiser, P., et al. Identifying the origin of thermal modulation of exchange bias in $MnPS_3/Fe_3GeTe_2$ van der Waals heterostructures. *Advanced Materials*, **2024**, 2403685.

[20] Puthirath Balan, A.; Kumar, A.; Scholz, T., et al. Harnessing van der Waals $CrPS_4$ and surface oxides for nonmonotonic preset field induced exchange bias in Fe_3GeTe_2. *ACS Nano*, **2024**, *18* (11), 8383-8391.

[21] Chakraborty, A.; Srivastava, A. K.; Sharma, A. K., et al. Magnetic skyrmions in a thickness tunable 2D ferromagnet from a defect driven Dzyaloshinskii–Moriya interaction. *Advanced Materials*, **2022**, *34* (11), 2108637.

[22] Sun, W.; Wang, W.; Li, H., et al. $LaBr_2$ bilayer multiferroic moiré superlattice with robust magnetoelectric coupling and magnetic bimerons. *npj Computational Materials*, **2022**, *8* (1), 159.

[23] Bhukta, M.; Dohi, T.; Bharadwaj, V. K., et al. Homochiral antiferromagnetic merons, antimerons and bimerons realized in synthetic antiferromagnets. *Nature Communications*, **2024**, *15* (1), 1641.

[24] Wang, X. S.; Qaiumzadeh, A.; Brataas, A. Current-driven dynamics of magnetic hopfions. *Physical Review Letters*, **2019**, *123* (14), 147203.

[25] Zheng, F.; Kiselev, N. S.; Rybakov, F. N., et al. Hopfion rings in a cubic chiral

magnet. *Nature*, **2023**, *623* (7988), 718-723.

[26] Jiang, W.; Zhang, X.; Yu, G., et al. Direct observation of the skyrmion Hall effect. *Nature Physics*, **2017**, *13* (2), 162-169.

[27] Shen, L.; Li, X.; Xia, J., et al. Dynamics of ferromagnetic bimerons driven by spin currents and magnetic fields. *Physical Review B*, **2020**, *102* (10), 104427.

[28] Amoroso, D.; Barone, P.; Picozzi, S. Spontaneous skyrmionic lattice from anisotropic symmetric exchange in a Ni-halide monolayer. *Nature Communications*, **2020**, *11* (1), 5784.

[29] Grebenchuk, S.; Mckeever, C.; Grzeszczyk, M., et al. Topological spin textures in an insulating van der Waals ferromagnet. *Advanced Materials*, **2024**, *36* (24), 2311949.

[30] Lv, X.; Lv, H.; Huang, Y., et al. Distinct skyrmion phases at room temperature in two-dimensional ferromagnet Fe_3GaTe_2. *Nature Communications*, **2024**, *15* (1), 3278.

[31] Schmitt, M.; Denneulin, T.; Kovács, A., et al. Skyrmionic spin structures in layered Fe_5GeTe_2 up to room temperature. *Communications Physics*, **2022**, *5* (1), 254.

[32] Ji, Y.; Yang, S.; Ahn, H.-B., et al. Direct observation of room-temperature magnetic skyrmion motion driven by ultra-low current density in van der Waals ferromagnets. *Advanced Materials*, **2024**, *36* (21), 2312013.

[33] Zhang, H.; Shao, Y.-T.; Chen, X., et al. Spin disorder control of topological spin texture. *Nature Communications*, **2024**, *15* (1), 3828.

[34] Lu, X.; Fei, R.; Zhu, L., et al. Meron-like topological spin defects in monolayer $CrCl_3$. *Nature Communications*, **2020**, *11* (1), 4724.

[35] Shen, Z.; Xue, Y.; Wu, Z., et al. Enhanced Curie temperature and skyrmion stability by strain in room temperature ferromagnetic semiconductor CrISe monolayer. *Applied Physics Letters*, **2022**, *121* (20), 202402.

[36] Du, W.; Dou, K.; He, Z., et al. Spontaneous magnetic skyrmions in single-layer $CrInX_3$ (X = Te, Se). *Nano Letters*, **2022**, *22* (8), 3440-3446.

[37] Gorkan, T.; Das, J.; Kapeghian, J., et al. Skyrmion formation in Ni-based Janus dihalide monolayers: Interplay between magnetic frustration and Dzyaloshinskii-Moriya interaction. *Physical Review Materials*, **2023**, *7* (5), 054006.

[38] Wang, Z.-Q.; Xue, F.; Qiu, L., et al. Switching intrinsic magnetic skyrmions with

controllable magnetic anisotropy in van der Waals multiferroic heterostructures. *Nano Letters*, **2024**, *24* (14), 4117-4123.

[39] Mühlbauer, S.; Binz, B.; Jonietz, F., et al. Skyrmion lattice in a chiral magnet. *Science*, **2009**, *323* (5916), 915-919.

[40] Soumyanarayanan, A.; Raju, M.; Gonzalez Oyarce, A. L., et al. Tunable room-temperature magnetic skyrmions in Ir/Fe/Co/Pt multilayers. *Nature Materials*, **2017**, *16* (9), 898-904.

[41] Xu, C.; Chen, P.; Tan, H., et al. Electric-field switching of magnetic topological charge in type-I multiferroics. *Physical Review Letters*, **2020**, *125* (3), 037203.

[42] Yuan, J.; Yang, Y.; Cai, Y., et al. Intrinsic skyrmions in monolayer Janus magnets. *Physical Review B*, **2020**, *101* (9), 094420.

[43] Liang, J.; Wang, W.; Du, H., et al. Very large Dzyaloshinskii-Moriya interaction in two-dimensional Janus manganese dichalcogenides and its application to realize skyrmion states. *Physical Review B*, **2020**, *101* (18), 184401.

[44] Wang, B.; Zhang, X.; Zhang, Y., et al. Prediction of a two-dimensional high-T_C f-electron ferromagnetic semiconductor. *Materials Horizons*, **2020**, *7* (6), 1623-1630.

[45] Tan, H.; Shan, G.; Zhang, J. Prediction of novel two-dimensional room-temperature ferromagnetic rare-earth material - GdB_2N_2 with large perpendicular magnetic anisotropy. *Materials Today Physics*, **2022**, *24* 100700.

[46] Sheng, K.; Chen, Q.; Yuan, H.-K., et al. Monolayer CeI_2: An intrinsic room-temperature ferrovalley semiconductor. *Physical Review B*, **2022**, *105* (7), 075304.

[47] You, H.; Ding, N.; Chen, J., et al. Gadolinium halide monolayers: a fertile family of two-dimensional 4f magnets. *ACS Applied Electronic Materials*, **2022**, *4* (7), 3168-3176.

[48] Sheng, K.; Yuan, H. K.; Wang, Z. Y. Monolayer gadolinium halides, GdX_2 (X = F, Cl, Br): intrinsic ferrovalley materials with spontaneous spin and valley polarizations. *Physical Chemistry Chemical Physics*, **2022**, *24* (6), 3865-3874.

[49] Bai, Y.; Wu, Y.; Jia, C., et al. Two-dimensional 4f magnetic $EuSn_2X_2$ (X = P, As) monolayers: A first-principles study. *Applied Physics Letters*, **2023**, *123* (1), 012401.

[50] Hirschberger, M.; Nakajima, T.; Gao, S., et al. Skyrmion phase and competing

magnetic orders on a breathing kagomé lattice. *Nature Communications*, **2019**, *10* (1), 5831.

[51] Ye, C.; Li, L.-L.; Shu, Y., et al. Generation and manipulation of skyrmions and other topological spin structures with rare metals. *Rare Metals*, **2022**, *41* (7), 2200-2216.

[52] Xu, J.; Wang, L.; Xi, L., et al. Spontaneous topological (anti)meron chains in the domain walls of centrosymmetric rare-earth magnet. *Advanced Functional Materials*, **2024**, *34* (22), 2314127.

[53] Shao, Q.; Liu, Y.; Yu, G., et al. Topological Hall effect at above room temperature in heterostructures composed of a magnetic insulator and a heavy metal. *Nature Electronics*, **2019**, *2* (5), 182-186.

[54] Hong, Y. L.; Liu, Z.; Wang, L., et al. Chemical vapor deposition of layered two-dimensional $MoSi_2N_4$ materials. *Science*, **2020**, *369* (6504), 670-674.

[55] Mortazavi, B.; Javvaji, B.; Shojaei, F., et al. Exceptional piezoelectricity, high thermal conductivity and stiffness and promising photocatalysis in two-dimensional $MoSi_2N_4$ family confirmed by first-principles. *Nano Energy*, **2021**, *82* 105716.

[56] Wang, L.; Shi, Y.; Liu, M., et al. Intercalated architecture of MA_2Z_4 family layered van der Waals materials with emerging topological, magnetic and superconducting properties. *Nature Communications*, **2021**, *12* (1), 2361.

[57] He, C.; Xu, C.; Chen, C., et al. Unusually high thermal conductivity in suspended monolayer $MoSi_2N_4$. *Nature Communications*, **2024**, *15* (1), 4832.

[58] Latychevskaia, T.; Bandurin, D. A.; Novoselov, K. S. A new family of septuple-layer 2D materials of $MoSi_2N_4$-like crystals. *Nature Reviews Physics*, **2024**, *6* (7), 426-438.

[59] Kulish, V. V.; Huang, W. Single-layer metal halides MX_2 ($X = Cl, Br, I$): stability and tunable magnetism from first principles and Monte Carlo simulations. *Journal of Materials Chemistry C*, **2017**, *5* (34), 8734-8741.

[60] Mermin, N. D.; Wagner, H. Absence of ferromagnetism or antiferromagnetism in one- or two-dimensional isotropic Heisenberg models. *Physical Review Letters*, **1966**, *17* (22), 1133-1136.

[61] Zhang, S.; Xu, R.; Duan, W., et al. Intrinsic half-metallicity in 2D ternary

chalcogenides with high critical temperature and controllable magnetization direction. *Advanced Functional Materials*, **2019**, *29* (14), 1808380.

[62] Ashton, M.; Gluhovic, D.; Sinnott, S. B., et al. Two-dimensional intrinsic half-metals with large spin gaps. *Nano Letters*, **2017**, *17* (9), 5251-5257.

[63] Ma, A. N.; Wang, P. J.; Zhang, C. W. Intrinsic ferromagnetism with high temperature, strong anisotropy and controllable magnetization in the CrX (X = P, As) monolayer. *Nanoscale*, **2020**, *12* (9), 5464-5470.

[64] Frey, N. C.; Kumar, H.; Anasori, B., et al. Tuning noncollinear spin structure and anisotropy in ferromagnetic nitride MXenes. *ACS Nano*, **2018**, *12* (6), 6319-6325.

[65] Kim, K.; Lim, S. Y.; Lee, J.-U., et al. Suppression of magnetic ordering in XXZ-type antiferromagnetic monolayer $NiPS_3$. *Nature Communications*, **2019**, *10* (1), 345.

[66] Kang, S.; Kim, K.; Kim, B. H., et al. Coherent many-body exciton in van der Waals antiferromagnet $NiPS_3$. *Nature*, **2020**, *583* (7818), 785-789.

[67] Li, P.; Yu, D.; Liang, J., et al. Topological spin textures in 1T-phase Janus magnets: Interplay between Dzyaloshinskii-Moriya interaction, magnetic frustration, and isotropic higher-order interactions. *Physical Review B*, **2023**, *107* (5), 054408.

[68] Berg, B.; Lüscher, M. Definition and statistical distributions of a topological number in the lattice O(3) σ-model. *Nuclear Physics B*, **1981**, *190* (2), 412-424.

[69] Du, W. H.; He, Z. L.; Dou, K. Y., et al. Chiral magnetic quasiparticles with zero topological charge in 2D lattice. *Advanced Functional Materials*, **2024**, 2400971.

[70] Wang, D.-S.; Wu, R.; Freeman, A. J. First-principles theory of surface magnetocrystalline anisotropy and the diatomic-pair model. *Physical Review B*, **1993**, *47* (22), 14932-14947.

[71] Moon, K.-W.; Yoon, J.; Kim, C., et al. Existence of in-plane magnetic skyrmion and its motion under current flow. *Physical Review Applied*, **2019**, *12* (6), 064054.

[72] Sun, W.; Wang, W.; Li, H., et al. Controlling bimerons as skyrmion analogues by ferroelectric polarization in 2D van der Waals multiferroic heterostructures. *Nature Communications*, **2020**, *11* (1), 5930.

[73] Zhang, X.; Xia, J.; Shen, L., et al. Static and dynamic properties of bimerons in a frustrated ferromagnetic monolayer. *Physical Review B*, **2020**, *101* (14), 144435.

[74] Zhang, S.; Li, Z. Roles of nonequilibrium conduction electrons on the magnetization dynamics of ferromagnets. *Physical Review Letters*, **2004**, *93* (12), 127204.

[75] Menezes, R. M.; Mulkers, J.; Silva, C. C. D. S., et al. Deflection of ferromagnetic and antiferromagnetic skyrmions at heterochiral interfaces. *Physical Review B*, **2019**, *99* (10), 104409.

[76] Thiele, A. A. Steady-state motion of magnetic domains. *Physical Review Letters*, **1973**, *30* (6), 230-233.

[77] Han, S. U.; Kim, W.; Kim, S. K., et al. Tunable domain-wall skyrmion Hall effect driven by a current and a magnetic field. *Physical Review B*, **2024**, *109* (1), 014404.

[78] Boulle, O.; Malinowski, G.; Kläui, M. Current-induced domain wall motion in nanoscale ferromagnetic elements. *Materials Science and Engineering: R: Reports*, **2011**, *72* (9), 159-187.

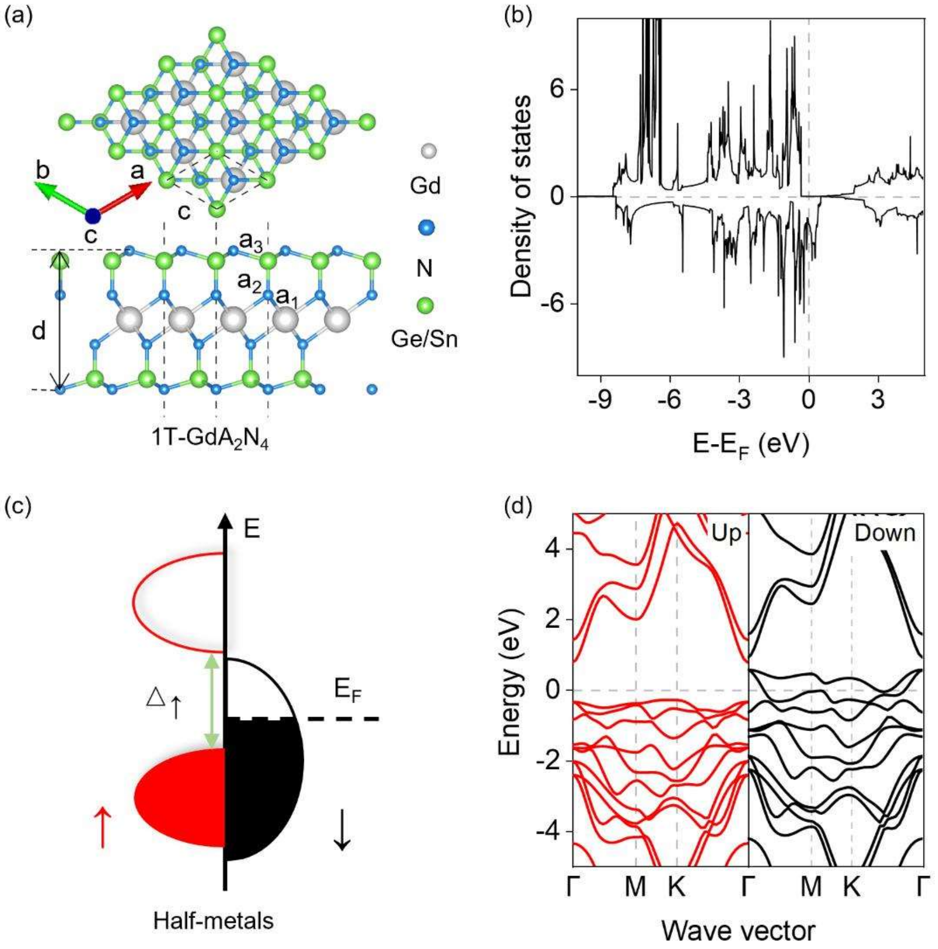

Figure 1 The electronic structure of the 1T-GdA$_2$N$_4$ monolayer: (a) the top and side views of crystal structure, where the dashed box represents the primitive cell; (b) the DOS; (c) the schematic of DOS, where $\triangle_{\uparrow}$ represents bandgap values of spin-up channel; (d) the spin resolved band structure.

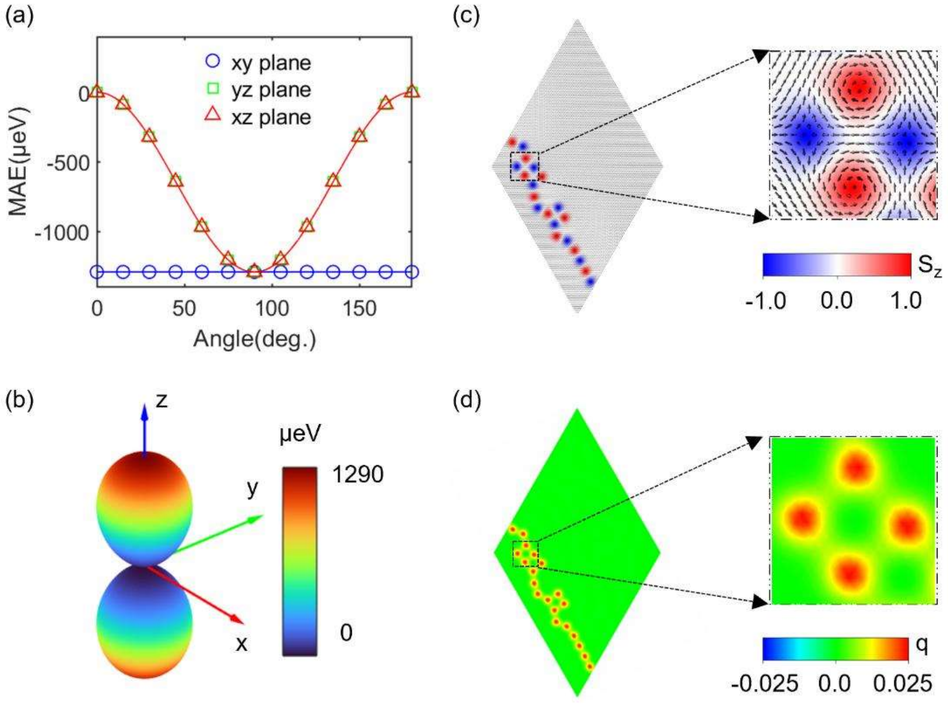

Figure 2 Magnetic anisotropy and the magnetic structures of monolayer $GdGe_2N_4$: (a) angular dependence of MAE in the *xy*, *yz*, and *xz* planes; (b) the MAE in the whole space; (c-d) topological spin textures and topological charge density at zero external magnetic field.

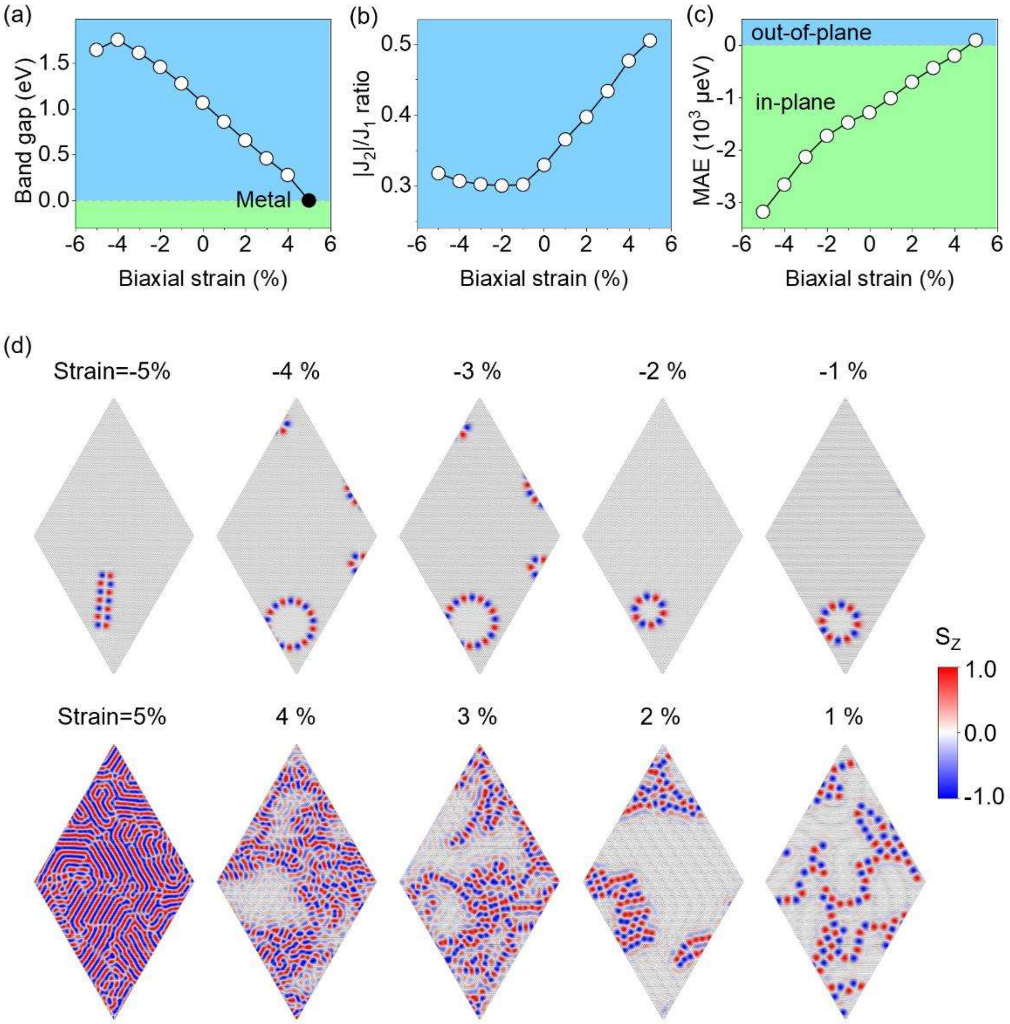

Figure 3 Biaxial strain dependence of the electronic and magnetic properties of the monolayer GdGe$_2$N$_4$: (a) strain dependence of the bandgap values of the spin-up channel (solid marker highlights the zero gap, i.e., the metallic state); (b) strain dependence of magnetic frustration ratio $|J_2|/J_1$; (c) strain dependence of the MAE; (d) strain dependence of topological spin textures at zero external magnetic field.

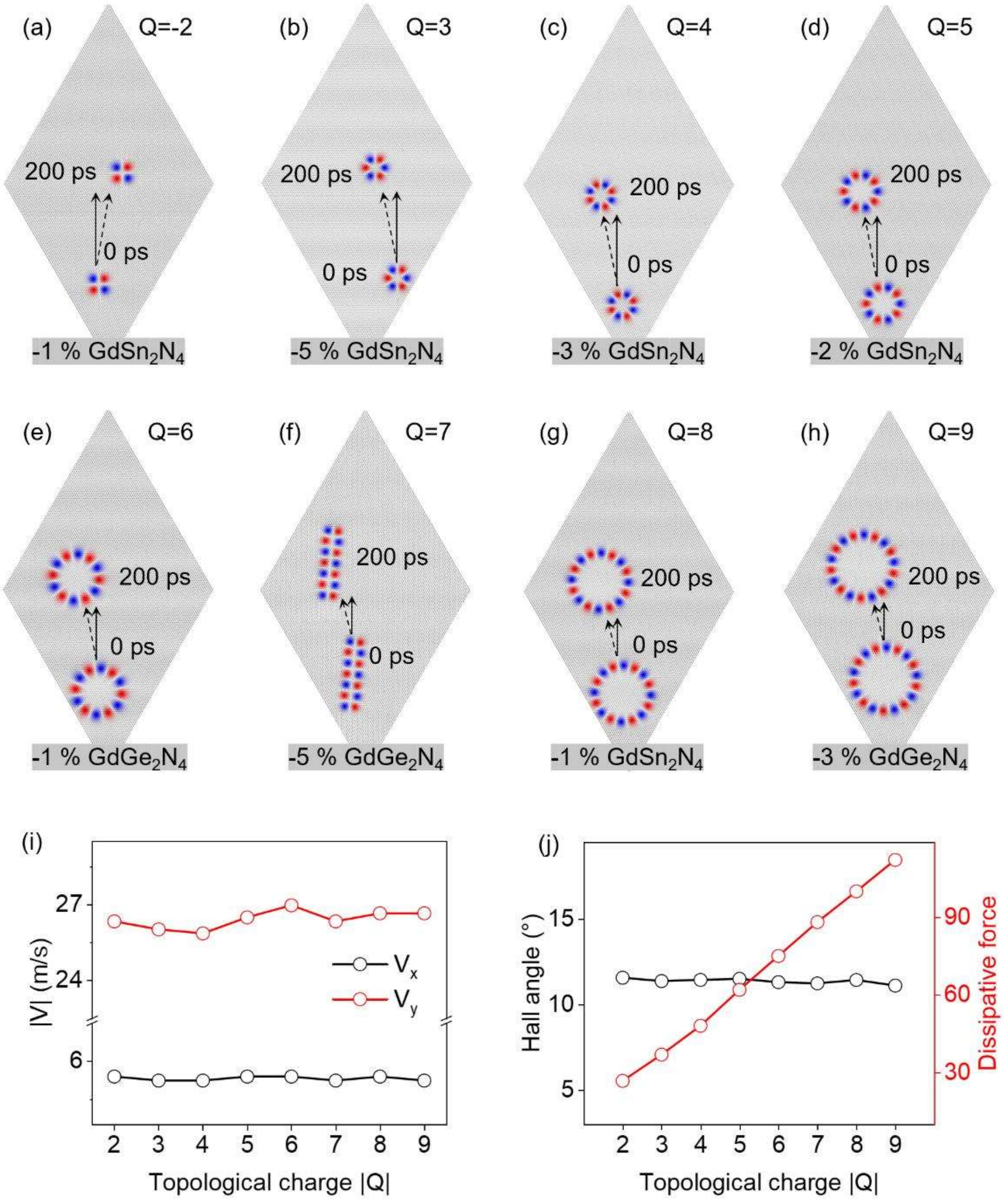

Figure 4 The spin-polarized current driven motion of the bimerons clusters in half-metallic monolayer GdA$_2$N$_4$ under different biaxial strain at zero external field: (a-h) the snapshots of the bimerons clusters driven by 100% spin-polarized current along *y* axis, where the solid line represents the direction of spin-polarized current, and the dotted line represents the direction of topological spin textures drift; (i) the drift velocity component along *x* and *y* directions; (j) the Hall angle and dissipative force of the bimerons clusters with different topological charges Q.